Electronic structure of noncentrosymmetric B20 compound HfSn and tuning of multifold band-crossing points

Dijana Milosavljević [1,*] Helge Rosner,[2] and Annika Johansson [1]
[1]*Max Planck Institute of Microstructure Physics, 06120 Halle (Saale), Germany*
[2]*Max Planck Institute for Chemical Physics of Solids, 01187 Dresden, Germany*

(Received 25 December 2023; accepted 9 July 2024; published 12 August 2024)

We present a detailed theoretical study of the electronic structure of hafnium tin HfSn crystallizing in a B20 structure, renowned for the diversity of physical and peculiar topological properties. The chiral crystal structure of these materials protects multifold band crossings located at high-symmetry points. We employ density functional methods to reveal basic features of the band structure and Fermi surface topology of HfSn, on top of which a tight-binding model is built. The compound exhibits a fourfold band crossing pinned at the Γ point. We investigate routes that can shift such crossings towards the Fermi level, offering a way to possibly tune the compound's properties. Specifically, we show that the energy position of the fourfold crossing can be easily manipulated via external perturbations such as strain and pressure. Considering that this point carries a topological charge larger than 1, such tuning is of great importance. We anticipate that the approach presented in the current study can be utilized to investigate symmetry-protected crossings in a wide class of materials.

DOI: 10.1103/PhysRevResearch.6.033157

I. INTRODUCTION

The synthesis and investigation of functional materials not available in nature are imperative for new technological developments and advancement in various disciplines. An important criterion is that the crystal structures of these novel materials are as simple as possible, but still host a wide spectrum of peculiar physical and chemical properties. This condition is fulfilled in the compounds with the noncentrosymmetric B20 crystal structure, which has a simple cubic unit cell and, as symmetry elements, screw and threefold rotations only [1]. The B20 family, named after their crystal structure, is an exciting class of materials in condensed-matter physics. Among the representatives of this family, there are metals [2], semiconductors [3], Kondo insulators [3], and superconductors [4]. Besides the conventional paramagnetic, diamagnetic, and ferromagnetic states, the B20-type members can exhibit chiral magnetic order featuring nontrivial chiral vortex-line spin textures and skyrmions [5]. Moreover, "nonmagnetic" ones display three-, four-, and sixfold degenerate band crossings pinned at high-symmetry points with topological charges greater than unity [6]. On top of the intriguing physical properties, a few members have already been recognized as stable electrocatalysts for hydrogen evolution reaction [7].

Whereas most of the literature on the B20 compounds focuses on monosilicides and monogermanides with transition metals from the seventh and eighth groups of the periodic table [8], scant attention has been devoted to the B20 structure compound with a transition metal of the fourth group. The first known compound associated with this particular subclass of the rich B20 family is HfSn [9]. In light of the extraordinary mechanical, reflectory, and high-corrosion resistance properties of Hf, investigation of its binary compounds is valuable. It is noteworthy that HfC is on the list of the most refractory materials under atmospheric pressure predicted to have the highest melting points [10]. In addition, the monolayers of HfC are predicted to be quantum spin Hall insulators by applying external in-plane strain, qualifying them as potential candidates for spintronics applications [11].

The wealth of existing applications of hafnium and its binary compounds and the uniqueness of the B20 family motivated us to systematically investigate the properties of HfSn. To the best of our knowledge, there are no experimental reports on the electronic structure properties of this compound. While in the literature there exist density functional theory (DFT) calculations of the band structure of HfSn published in [12] and in the material project database [13], many features associated with it have not yet been established, opening a space for further investigation. Moreover, in our paper, we carefully examine the influence of spin-orbit coupling. Also, very little attention has been dedicated to the other two four-group transition-metal B20 representatives, HfSb and ZrSb. As an illustration, HfSb has been proposed to be a semimetal exhibiting the quantum anomalous Hall phase [14], and ZrSb is an insulator found to be trivial [14].

In the present work, we report an extensive computational study of HfSn by means of DFT and the subsequent modeling approach. The so-derived tight-binding Hamiltonian is

*Contact author: dijana.milosavljevic@mpi-halle.mpg.de

employed for the investigation of the topological properties of this material. An ultimate goal of the paper is to construct a clear physical picture of the electronic structure of HfSn, contributing to a better comprehension of B20 compounds, in particular, those with a transition metal from the fourth group, which have been underexamined so far.

The HfSn phase was first reported by Schob *et al.* [9] to be stable over a narrow temperature range around 1000 °C. In the subsequent publication of Tsyganova *et al.* [15], the Hf-Sn phase diagram, constructed based on the differential thermal analysis and x-ray diffraction results, did not contain the HfSn phase. Contrasted with this result, Romaka *et al.* [16] established the binary Hf-Sn system phase diagram containing HfSn, Hf_5Sn_4, $HfSn_2$, and Hf_5Sn_3. Further experiments on related Hf-Ni-Sn systems validated the existence of the HfSn phase (Stadnyk *et al.* [17]). Tang *et al.* [18] disregard the HfSn phase in the thermodynamic modeling, but still report the first-principles results of its crystal structure, indirectly pointing to the occurrence of HfSn. It is important to emphasize that in the current paper, we do not address the stability of the HfSn phase. Instead, we take the first crystallographic report by Schob *et al.* [9] and employ it as a starting point for all of the calculations presented in the current work.

The work is organized as follows. In Sec. II, we establish the theoretical methods utilized in the current study. Section III contains a brief description of the experimental crystal structure [9]. In Sec. IV A, we report the electronic structure of HfSn obtained by means of DFT. We use this information to explore how external perturbations such as hydrostatic pressure (Sec. IV B), and uniaxial strain and doping (Sec. IV C), can be utilized to tune points of interest in the electronic structure, namely, multifold band crossings. In Sec. IV D, we construct a tight-binding model which is then used to investigate the topological properties of these points.

II. METHODS

The calculations are performed by employing the local density approximation (LDA) and generalized gradient approximation (GGA) for the exchange-correlation functional as implemented in the Full Potential Local Orbital (FPLO) code [19] and Vienna Ab Initio Simulation Package (VASP) [20–22], within the projector-augmented plane-wave (PAW) method. We use the Perdew-Wang [23] and Perdew-Burke-Ernzerhof [24] methods for LDA and GGA, respectively. For VASP, we use the parametrization of Ceperly-Alder [25] for the LDA, while the GGA parametrization is the same as in the FPLO code. The spin-orbit coupling (SOC) is treated nonperturbatively in FPLO and in a second variational scheme in VASP. Starting from the experimental crystal structure [9], we relax the atomic positions until the forces reach a value of less than 10^{-3} eV/Å. In addition to the atomic positions, we fully relax the volume of the unit cell of the HfSn. We downfold our FPLO calculations on a Wannier functions (WFs) basis incorporating Hf $5d$, $6p$, and Sn $5p$ orbitals, with the requirement of maximum localizations. Furthermore, we use the output of our bulk VASP calculations to construct the maximally localized (ML) WFs employing the WANNIER90 [26] code. The so-obtained ML-WFs are used to calculate the total and band-resolved Berry curvature. The topological charges are calculated utilizing the WANNIERTOOLS package [27]. We plot the band-resolved Berry curvature with the help of the WANNIERBERRI code [28]. A well-converged k mesh of $12 \times 12 \times 12$ k points in the whole Brillouin zone is employed. For VASP calculations, we set the k-point grid to $12 \times 12 \times 12$, and the convergence of the total energy is 10^{-6} eV.

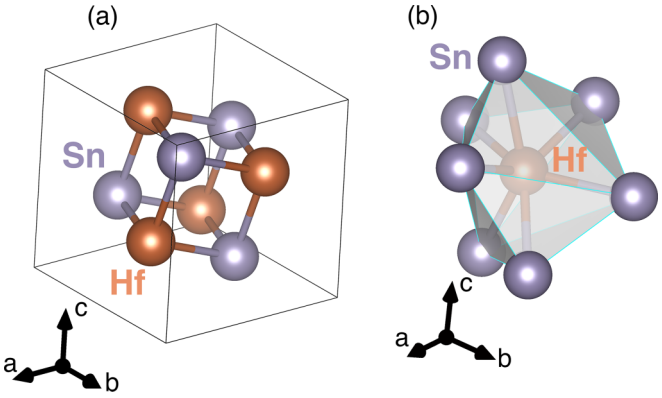

FIG. 1. (a) The unit cell of the B20 crystal structure of HfSn. The orange atoms in the unit cell depict Hf atoms and purple atoms illustrate Sn atoms. (b) Coordination polyhedron of an Hf atom. Six Sn atoms are located at the distance of 2.99 Å and one is at 3 Å (or 7 equidistant, depending on error bars).

III. CRYSTAL STRUCTURE

The crystal structure of HfSn is described by a B20 Strukturbericht designation, a name that accounts for binary compounds that crystallize in the space group $P2_13$ (no. 198 in the International Table). A distinguished feature of this family is the lack of mirror and inversion symmetry, resulting in a chiral crystal structure. Thus, in total, this space group contains 12 symmetry operations: twofold and threefold screw rotations and simple threefold rotations. In a simple cubic unit cell, there are four atoms of each species located at the $4a$-type Wyckoff positions determined by the parameters $x_{\mathrm{Hf}} = 0.155$ and $x_{\mathrm{Sn}} = 0.845$ [9] for Hf and Sn atoms, respectively (see Fig. 1). The experimental room-temperature lattice parameter is $a = 5.594$ Å [9]. Each atom, Hf and Sn, is bonded to six nearest neighbors (NNs) of opposite kinds at a distance of 2.99 Å and one at 3.00 Å. If one takes into account experimental uncertainty, there are seven equidistant NNs at a distance $a\sqrt{(3)}/[1+\sqrt{(5)}] = 2.99$ Å resulting in an "ideal" B20 structure [29]. The next-nearest neighbors (NNNs) of each atomic species are atoms of the same kind whose separation is equal to 3.45 Å (for all six atoms).

IV. RESULTS

A. Electronic structure

First, we present the analysis of the density of states (DOS) and electronic band structure. In Fig. 2, the total and atom-resolved density of states of HfSn are shown. From Fig. 2(a), it can be deduced that the density of states at the Fermi level E_F is approximately 9.0 states/(eV cell). This result is comparable to 10.5 states/(eV cell) obtained for CrGe [30]

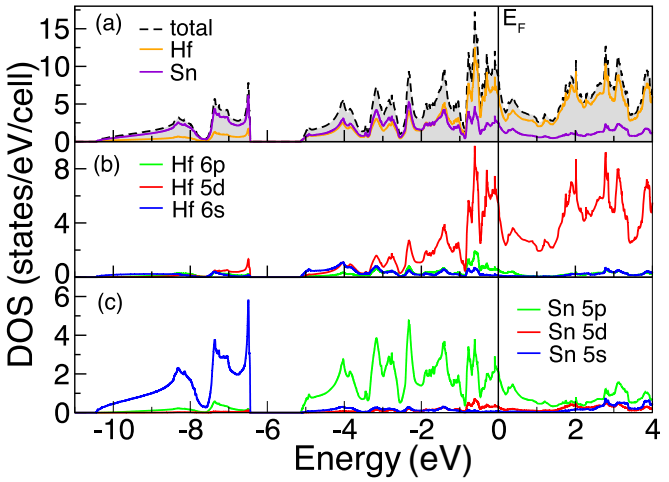

FIG. 2. Calculated LDA total and atom-resolved partial electronic densities of states of the HfSn. The Fermi level is at zero energy and marked by a full black line.

with the FPLO code. In both systems, such a high value of DOS is caused by the presence of many bands crossing the Fermi level. The valence-band complex is dominated by Sn states with sizable contribution of Hf states above −1.5 eV [see purple and orange lines in Fig. 2(a)].

The orbital-resolved DOS shown in Figs. 2(b) and 2(c) indicate that Hf and Sn 5*d* states contribute mainly in the energy window from −5 to 4 eV. The same also applies to the 6*p* and 5*p* block of Hf and Sn, respectively. Specifically, the Hf 5*d* states contribute about two-thirds of states at the Fermi level E_F and Sn 5*p* contributes about one-quarter. Additionally, the Hf 6*p* states are present at E_F with 6% compared to the total DOS and Sn 5*d* states with 3%. The contribution of all other states is about 1% and is therefore negligible. This analysis is of major importance because it guides the construction of a tight-binding model.

We stress that two different exchange-correlation functionals (LDA versus GGA) qualitatively lead to the same results. Also, two codes (FPLO and VASP) yield the same qualitative behavior. Hence, in the discussion below, we mainly focus on the FPLO results. The bulk band structure of HfSn for the experimental crystal structure [9] is shown in Fig. 3. The overall shape and dispersion of the bands resemble that previously calculated for HfSn [12], providing a justification for our calculations. However, in addition to this, we dedicate special attention to the peculiarities of the band-structure-like crossings and their energy separation from the Fermi level. This is an important issue to revisit because it could possibly offer a mechanism to modify the compound properties by external influence. In the energy range from -5.3 to 1.4 eV, overall there are 30 bands (which are easiest to see along the Γ*M* direction). These states group into sets of subbands which become two- and fourfold degenerate in the Brillouin zone center (Γ point). There exist five subsets of twofold and fourfold degeneracies. At the Brillouin zone corner (*R* point), the bands exhibit peculiar two- and sixfold degeneracies. At the Brillouin zone boundary, all states are twofold degenerate. The presence of multifold degenerate bands at high-symmetry points is a distinguished characteristic of the

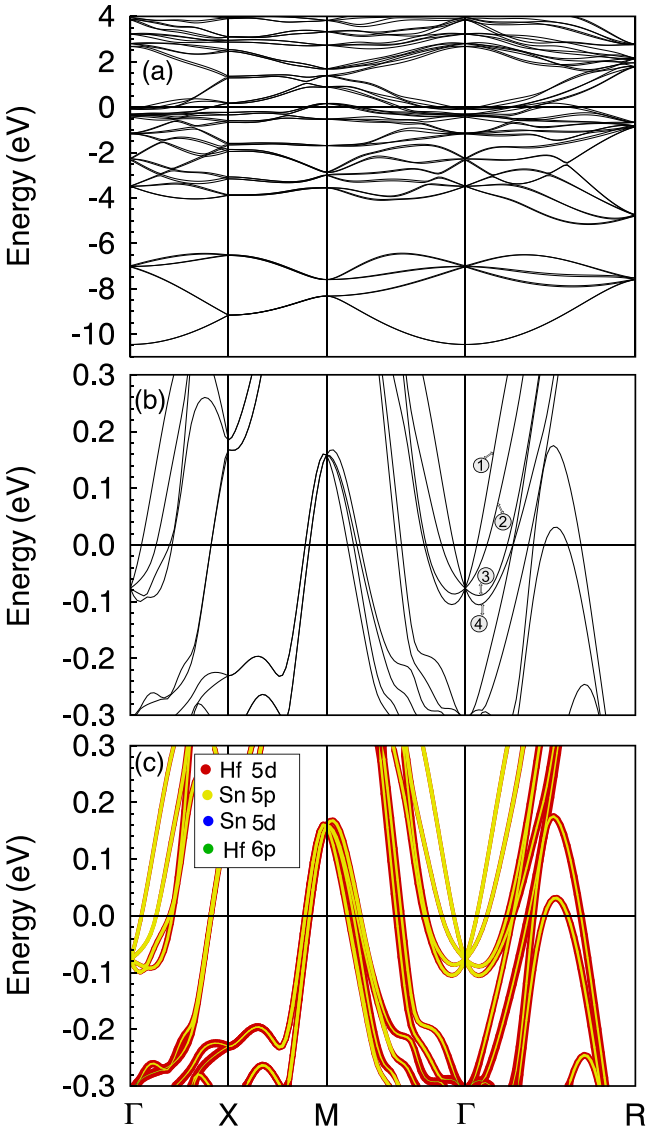

FIG. 3. (a) Calculated LDA band structure of HfSn with SOC. (b) Zoom of the band structure around the Fermi level E_F. Numbers 1–4 denote the bands forming a fourfold degenerate point just below the E_F. (c) Calculated orbital band character in the vicinity of E_F: Hf 5*d* (red), Hf 6*p* (green), Sn 5*d* (blue), and Sn 5*p* (yellow).

whole family of B20 compounds. This feature is a direct consequence of the structural chirality of the respective real-space lattice and the peculiar symmetries of the B20 compounds. Owing to the nonsymmorphic C_2 rotation and time-reversal symmetry, the analysis of the linearized **k**·**p** Hamiltonian reveals the stability of the degeneracies up to higher orders in **k**·**p** [31]. The multiplicity of band crossings on high-symmetry points is determined by the dimensionality of the irreducible representation of the little groups [32]. For the case with SOC, at Γ there are representations of dimensionality 2 and 4, and at *R*, 2 and 6, resulting in twofold and fourfold degeneracies at Γ, and twofold and sixfold degeneracies at *R*, in agreement with our calculations. The fourfold crossings at Γ and sixfold crossings at *R* are observed in other chiral crystals from the B20 class, such as CoSi [33], CoGe [34], and PdGa [6].

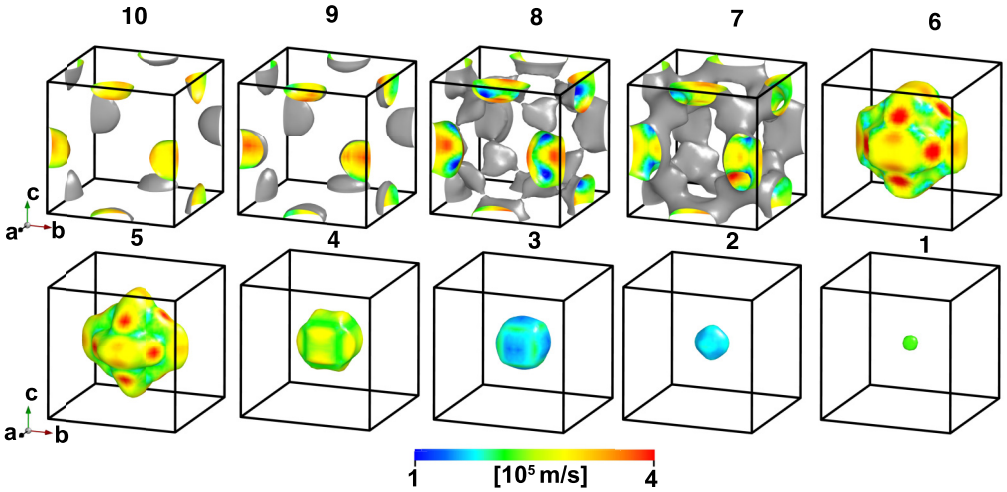

FIG. 4. The Fermi surfaces of HfSn with the Fermi velocities at various pockets depicted with color gradients. The calculations are presented for the experimental crystal structure with SOC.

A zoom around the Fermi level of the band structure at the Γ point reveals the fourfold degeneracy located 78 and 102 meV below the Fermi level in LDA and GGA, respectively [see Fig. 3(b) for LDA and the Appendix, Sec. 2, for GGA; Figs. 9 and 10]. These degenerate points are more than a factor of two closer to the Fermi level compared to the calculations without SOC (see the Appendix, Sec. 2; Figs. 9 and 10). At the *R* point, the sixfold degenerate point is significantly lower in energy in both LDA and GGA than the degenerate point at the Γ. Hence, we mainly focus on the properties of the electronic structure around the Γ point in the following. We find the energy position of the degenerate point at Γ to be sensitive on the optimization of the experimental crystal structure [9] (see below). The states in the energy region from −0.3 to 0.3 eV are characterized by a strong hybridization between Hf 5*d* and Sn 5*p* states [Fig. 3(c)]. The *d*-*p* admixture is frequently encountered in transition-metal intermetallic compounds, governing their electronic properties.

Our calculations for HfSn, with SOC included, reveal 10 Fermi surface sheets as depicted in Fig. 4 (labeled with numbers from 1 to 10). Six out of 10 Fermi sheets are electron pockets centered at Γ (two of them, labeled as 6 and 5 in Fig. 4, are of the octahedral shape, and four of them, labeled as 4, 3, 2, 1 in Fig. 4, are approximately spherical). Spherical sheets have moderately lower Fermi velocities compared to other sheets. In addition, there is one sheet that forms the webbed tunnel (7 in Fig. 4), with the remaining three (10, 9, 8) representing hole pockets located at the edges of the Brillouin zone.

As a next step, we perform structural optimization of the experimental structural data [9]. The optimization of the atomic coordinates only is followed by a full optimization of the unit cell. These calculations lead to an optimized structure which differs from the "ideal B20" structure in the sense that the seven nearest-neighbor distances (see Fig. 1) are not equal, not even approximately. Instead, there are three distinct distances denoted d_1, d_2, and d_3, respectively (see Table I). We find that the optimization of the crystal structure predominantly influences the position of the degenerate point, irrespective of the employed basis set (plane wave as implemented in VASP versus local orbitals in FPLO). Full optimization of the crystal structure moves the multifold point at Γ towards the Fermi level by approximately 22 meV in LDA (FPLO). In GGA (both codes), this behavior is opposite and the point moves away from the Fermi level by almost 33 meV compared to the experimental crystal structure [9] (see Table I). The difference in the optimized lattice parameters of about 0.02 Å in LDA and 0.03 Å in GGA between FPLO and VASP can be thoroughly ascribed to the different types of basis sets. Optimization of the atomic coordinates solely (not shown in Table I) also has an impact on the position of the degenerate point, just with a less pronounced shift, reduced by approximately a factor of two compared to the case when the structure is fully optimized. For further analysis, we make use of our LDA optimized parameters, which can be justified by the fact that LDA performs the best for elemental Sn over the GGA functionals [35]. Furthermore, it is established that the tendency of LDA to underestimate the lattice constants is smaller than the GGA overestimation of parameters [36].

B. Hydrostatic pressure

From Table I, it can be concluded that smaller lattice parameters in LDA and, consequently, smaller volumes lead to a shift of the degenerate point closer to the Fermi level. In a material, it is desirable that such band degeneracies occur in the vicinity or exactly at the Fermi level, in order to get a chance to investigate peculiar transport and topological properties originating from the electronic states around these points. Hence, it is of the utmost importance to identify all possible routes by which such band crossing can be located at E_F. Our results illustrate that volume compression acts in favor of achieving this effect. In reality, volume reduction can be achieved by application of hydrostatic pressure. Therefore, this result prompts an investigation of the hydrostatic pressure influence on the properties of HfSn, in particular the position of the fourfold degenerate point at Γ. In the following, we report on the hydrostatic compression studies on HfSn. In Fig. 5, we show the separation of the degenerate point at Γ from the Fermi level E_F as a function of the compressed

TABLE I. Lattice parameter a (Å), distances d_1, d_2 and d_3 (Å), energy separation t (meV), and volume V (Å^3) obtained by full structural optimization employing the FPLO and VASP codes with various exchange-correlation functionals (LDA vs GGA). d_1, d_2, and d_3 denote the NN distances between Hf and Sn atoms (d_1 appearing once and d_2 and d_3 three times), t stands for the energy separation of the degenerate points at Γ from the Fermi level, and V is the volume obtained after structural optimization. The Wyckoff positions for Hf and Sn atoms are denoted with x_{Hf} and x_{Sn}, respectively. The values for the experimental crystal structure (Expt. [9]) are also presented.

	VASP		FPLO		Expt. [9] VASP		Expt. [9] FPLO	
	LDA	GGA	LDA	GGA	LDA	GGA	LDA	GGA
a	5.5368	5.6543	5.5555	5.6817	5.594		5.594	
d_1	2.882 × 1	2.935 × 1	2.890 × 1	2.949 × 1	2.990		2.990	
d_2	2.917 × 3	2.979 × 3	2.926 × 3	2.992 × 3				
d_3	3.045 × 3	3.114 × 3	3.058 × 3	3.131 × 3				
t	−41.17	−104.13	−56.12	−135.65	−51.10	−72.41	−78.33	−102.27
V	169.737	180.784	171.463	183.415	175.052		175.052	
x_{Hf}	0.144	0.143	0.144	0.143	0.155		0.155	
x_{Sn}	0.843	0.844	0.843	0.843	0.845		0.845	

volume. The minus sign indicates that the point of interest is still below E_F with a crossover at zero, after which it becomes positive. Compressing the volume, the nonsymmorphic band crossing gradually approaches E_F, and passes it at about 6% of volume compression, after which it continues to steadily move away. Upon application of a hydrostatic pressure, all initial symmetries in the system remain unaffected. The NN distances (d_1, d_2, d_3) linearly decrease with the increasing hydrostatic pressure. Accordingly, the whole crystal structure smoothly deforms under compression, yielding no signatures of deformations or electronic topological transitions. The two tiny, approximately spherical Fermi surfaces around the Γ point (1 and 2) vanish with the application of the critical hydrostatic pressure of about 6%.

To determine the bulk modulus and its derivative with respect to pressure, our calculated hydrostatic pressure data were fitted with the Birch-Murnaghan (BM) [37] equation of state (EOS). As a result of the BM fit, the bulk modulus and its pressure derivative are $B = 117$ GPa and $B' = 4.5$, respectively. In the literature, there are no experimental or theoretical reports that we can compare our results with. According to Ref. [38], which studies the elemental bulk modulus across the periodic table of elements, neither Hf nor Sn belong to the class of high bulk modulus materials. Hence, the value for HfSn is expected to be in the range typical for binary intermetallics [39], in agreement with our findings. We note that fitting the data with Vinet [37], Birch only, and Murnaghan only [40], the EOSs result in a small renormalization of the bulk modulus (by a maximum of 5 GPa). Employing the volume-pressure dependence [41], we estimate that 6% of the volume compression, required to locate the degeneracy at E_F, is equivalent to the application of hydrostatic pressure of about 8.5 GPa.

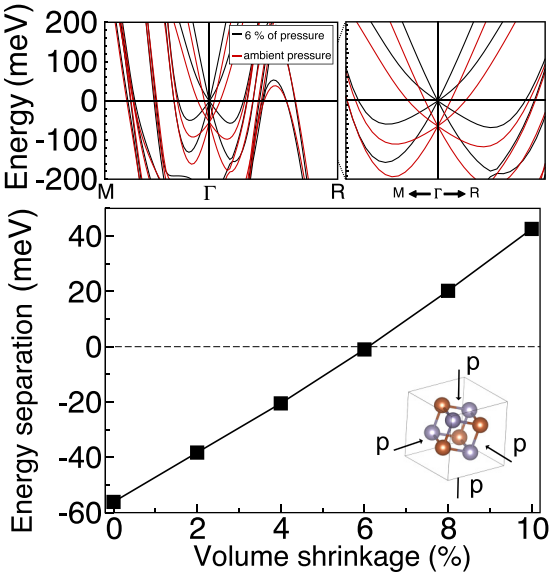

FIG. 5. Top panel: Band structure at ambient pressure and 6% of volume reduction corresponding to hydrostatic pressure of about 8.5 GPa. Main panel: Distance of the degenerate point at Γ from the Fermi level as a function of the volume compression by hydrostatic pressure application.

C. Uniaxial strain and chemical pressure

However, the hydrostatic pressure is not the only path to pinpoint the Fermi level at the degenerate point. To achieve this, uniaxial strain and doping can also be utilized as tuning tools. Compared to the hydrostatic pressure, strain is expected to lead to much stronger effects influencing not just the position of the bands, but also the band degeneracies due to the symmetry breaking [42]. First, a compressive strain along the [100] lattice direction is applied, lifting the original cubic crystal symmetry. Application of strain along [100] breaks the threefold rotational symmetry, all five simple and three screw operations, and, consequently, there is a lowering of the crystal symmetry from cubic to orthorombic. For the unstrained lattice parameters, our FPLO LDA optimized structure is exploited. Intrinsically, compression along the a axis leads to a tension along b and c with specific, material-dependent Poisson ratios. We assume an ideal Poisson ratio of 0.5, often employed to describe linear elastic materials. As illustrated in Fig. 6, uniaxial compressive strain results in a splitting of the fourfold degenerate point at Γ into two twofold degenerate points. At the R point, the native sixfold degenerate point with uniaxial strain transforms into three twofold crossings. The newly created pairs of twofold degeneracies at Γ behave

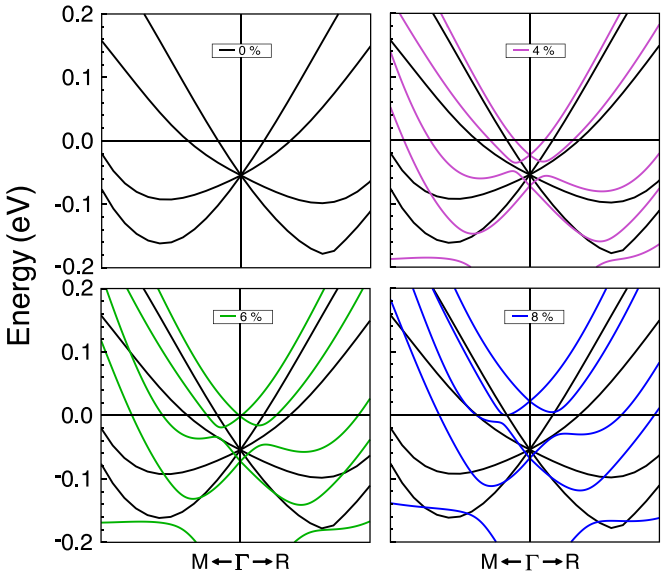

FIG. 6. Zoom of the band structure of HfSn around E_F under strain. Zero strain structure depicted in black is the FPLO LDA optimized structure. Purple, green, and blue curves correspond to 4%, 6%, and 8% of compressive uniaxial strain, respectively. Each panel highlights the band structure for one distinct and zero strain value.

distinctly upon increasing strain. While one pair stays mostly in the vicinity of the original fourfold degenerate point, the second pair experiences a notable shift in energy and, at about 6% of strain, it is situated at the Fermi level.

Creating off-stoichiometry at either the Hf or Sn site is an alternative route to control the band filling, and hence the position of the bands with respect to the Fermi level. This manipulation induces chemical pressure which resembles the effect of hydrostatic pressure in a nonuniform manner. As a first step, we investigate this effect in a rigid band approximation. Assuming a simple band shift within LDA, it is required to add approximately 0.1 electrons per unit cell to displace the degenerate point at the Fermi level (in GGA, this point is even further away from the Fermi level, so approximately a three times larger number of electrons needs to be added to accomplish the same effect). To improve the description of a chemical disorder, as a next step we employ a virtual crystal approximation (VCA), which considers not only the shift in the Fermi energy, but also the change in the potential traced to the modified number of electrons in the system [43]. In practice, in the VCA approach, the average charge at either the Sn or Hf site is reduced. We find that when introducing a deficiency at the Sn site $HfSn_x$ of about $x = 0.10$, the degenerate point is located at the Fermi level. This can be accomplished by substituting Sn atoms with Ge atoms ($HfSn_{1-x}Ge_x$). Both Sn and Ge are tetravalent atoms and have ionic radii which differ by almost 0.14 Å. Considering that Ge has smaller ionic radii compared to Sn, the volume of the unit cell is expected to decrease with this substitution, an effect which additionally influences the position of the bands, as previously demonstrated. As both effects act in the same way, the actual percentage of Sn atoms to be substituted is expected to be smaller than 10%. Equivalently, deficiency at the Hf site leads to a shift of the bands towards the Fermi level. The difference is that a slightly larger amount of Hf has to be substituted (at least 12% to achieve the same effect as 10% Sn substitution). Isovalent substitution of Hf with Zr is a possible mechanism as it does not introduce significant structural distortions due to the similarity of the ionic radii of Hf and Zr.

D. Construction of a tight-binding model

To complete the description of the compound, it is desirable to obtain a reliable tight-binding (TB) model that would not just reveal the main hopping mechanisms in the system, but also enable access to the topological properties. To achieve this, we construct a tight-binding model based on maximally localized Wannier functions that accurately reproduces the band structure obtained by means of DFT (see Figs. 7 and 8 in the Appendix, Sec. 1). As initial projectors for constructing the Wannier Hamiltonian, we employ Hf 5d (xy, yz, xz, x^2-y^2, z^2), 6p (x, y, z), and Sn 5p (x, y, z) orbitals. Due to the fact that the target bands in the vicinity of the Fermi level, essential for construction of the low-energy model, are strongly hybridized, one needs to set a large energy window while constructing the WFs. In addition, we have carefully examined the dependence of the results on the real-space distance at which the hoppings are cut off and the magnitude of the hoppings with respect to the specified threshold (both requirements ensure that the minimum number of hoppings, essential for the physics, are contained in the model). Both have to be large in order to reliably reproduce the DFT band structure. Due to the lack of inversion symmetry, all hopping parameters along arbitrary directions $\mathbf{r}$ and $-\mathbf{r}$ are allowed to differ in magnitude and sign. Our calculations reveal that nearest-neighbor (NN) coupling between Hf and Sn atoms is the dominant hopping regime in the compound. It is driven by a strong hybridization between Hf 5d and Sn 5p orbitals, as well as Hf 6p and Sn 5p states (see Tables II and III in the Appendix, Sec. 6). The hopping amplitudes from the Hf 5d to Sn 5p states are $t_{\mathrm{pd}} \approx 1.2$ eV (one out of seven possible coupling mechanisms). Interestingly, hopping to the Sn 5p states from the Hf 6p state is even larger compared to the d-p channel, and these are the parameters with the largest magnitude (≈1.7 eV). This is elucidated by the fact that the Hf 6p orbitals are extended enough to provide significant overlap with the neighboring p orbitals of Sn atoms. Moreover, the overlap between 5p and 6p orbitals of the same kind (p_x-p_x, p_y-p_y, p_z-p_z) is larger by a factor of two than the overlap between orbitals of different kinds. All the next-nearest-neighbor (NNN) hopping parameters are decreased compared to the NN ones, in agreement with the fact that the hopping magnitude decreases with increasing distance between the sites. It should be emphasized that NNN parameters cannot be neglected when building the model, signaling their important role in reliable compound description. Quite surprisingly, the long-range hopping parameters are of enormous importance in obtaining a reliable fit to the DFT band structure. The so-derived picture of the hopping regime of HfSn remains to hold with the inclusion of SOC, just with a renormalization of some of the parameters and introduction of imaginary components (see Tables IV and V in the Appendix, Sec. 6). In particular, the p-p overlaps in the NN coordination polyhedra are affected. This could be

attributed to the relativistic effects which have a tendency to contract the p orbitals to some extent.

Using a TB model Hamiltonian, we evaluate the band-resolved Berry curvature (BC) and the BC summed over the occupied states depicted in Figs. 13(a) and 13(b) (Appendix, Sec. 5), respectively. Our calculations illustrate that there is a large contribution to the Berry curvature when bands are near each other energetically. As the next step, the topological charges of the bands forming the fourfold degenerate point at the Γ point just below the E_F are evaluated. The dependence of the results on the radius of a sphere constructed around Γ is carefully examined. We find that the topological charges for the first to fourth bands are $+3$ (band 1), $+1$ (band 2), -1 (band 3), and -3 (band 4) [see notation in Fig. 3(b)]. The values for the topological charges and their distribution across bands agree well with those derived for CoGe [34] and CoSi [33] for their fourfold degenerate points located approximately 20 meV below E_F for both systems. The topological character of the fourfold degeneracy point identifies this point as a spin-3/2 Weyl node, in agreement with [34]. Multifold fermions at high-symmetry points, in particular fourfold spin-3/2 chiral Weyl fermions at Γ and sixfold Weyl fermions at R, are characteristic for B20 compounds and are expected to give rise to unique topology-related transport properties such as the chiral anomaly [44,45], nonlinear optical transport [12], pronounced orbital transport effects [46], circular photogalvanic effect [47], and helical magnetic effects [48]. Tuning the degeneracy points at Γ and R to the Fermi level enables the opportunity to modify and possibly enhance these transport effects.

V. SUMMARY AND CONCLUSION

In summary, we perform an extensive theoretical study of noncentrosymmetric HfSn, the first known member of the B20 family where a transition metal is from the fourth group. We investigate the band structure and Fermi surface utilizing DFT and a model approach to access the topological properties. Our results presented above show that there is a fourfold degenerate point at Γ located at a maximum of 0.1 eV below the Fermi level, which has spin-3/2 Weyl node character. Considering that this band energy is not tremendously large, it is possible to tune it across the Fermi level via external perturbations. Such a manipulation would conceivably lead to a spectrum of novel physical phenomena, such as chiral anomaly [45] and large nonlinear optical conductivity [12]. We demonstrate that the volume shrinkage caused by increasing hydrostatic pressure is driving the fourfold degeneracy towards the Fermi level, reaches it for about 6% of compression, and continues to relocate in the same manner. In contrast to hydrostatic pressure where the volume is isotropically compressed, the uniaxial strain allows selection of a specific lattice direction, enabling control over the breaking of the original symmetries of the crystal lattice. Applying the [100] strain on HfSn, we lift some symmetries and break fourfold degeneracy into two twofold subsets, one of which is driven across the Fermi level for strain of about 6%. Comparing pressure and strain, the hydrostatic pressure investigations are, at present, more applicable to HfSn due to the availability of powder samples only. However, constant advancements of the synthesis techniques may result in high-quality single crystals of HfSn in the near future, highlighting the significance of the uniaxial pressure study presented here. Creating off-stoichiometry has a considerable effect on the electronic structure of HfSn. The isoelectronic substitution of Sn by Ge shifts the Fermi level, and the fourfold point is at Γ for a Ge concentration of about 10%. Further investigations are required to understand how the disorder created by this perturbation influences other bands. Nevertheless, neither hydrostatic pressure nor chemical composition of the sample have an influence on the multiplicity of the band crossings occurring at high-symmetry points. They arise purely due to the symmetry elements of the respective chiral space group. The crucial factor capable of modifying this multiplicity is the symmetry breaking that can be realized by the application of uniaxial strain. All three ways of external tuning presented in the current work move the crossing up and down in energy, but only strain prompts a reduction of its degeneracy. Parametrization of a TB model reveals the dominant role of NN and NNN hoppings with non-negligible contribution of the higher-order terms. Although it remains to be seen whether this conclusion is generic across the whole family of B20 compounds, a consistent set of parameters derived in the current work undoubtedly can be utilized as a starting point to fit the band structure of a different system in the same class of compounds. This considerably speeds up the construction of an effective model.

The methodology presented in the current work is not specific to HfSn only, but can be equally applied to other members of the B20 family. It is particularly relevant to those compounds which have their symmetry-protected crossings within a few meV range from the Fermi level. Applying exactly the same approach, one obtains initial predictions about binding energies of the respective bands and energy window within which they can be shifted by different mechanisms of external perturbations. Our results demonstrate how DFT can be employed as a useful tool to qualitatively predict the outcome of complex experiments before they are performed and can help in the design of new experimental setups. Going beyond B20, many other space groups host symmetry-protected band crossings which can be approached in the same way as presented here, illustrating the generality of our findings.

ACKNOWLEDGMENTS

Computations were performed on the HPC systems Raven and Cobra at the Max Planck Computing and Data Facility (MP CDF). D.M. acknowledges application support provided by MP CDF.

APPENDIX

1. Wannier fit

Figures 7 and 8 show the comparison of the DFT LDA band structure (black) with the one from the Wannier function model (red). The green curve represents the TB approximation to the full WF model (red), where cutoff for the hoppings and magnitude threshold are taken into account. It is visible that the regions around the Fermi level are well reproduced (red

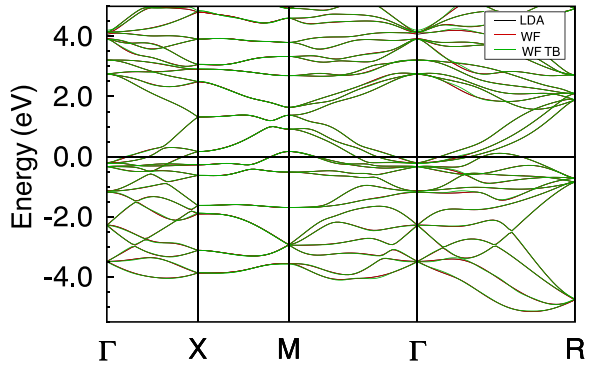

FIG. 7. Comparison of full DFT band structure with the one from the reduced Wannier model when SOC is not included.

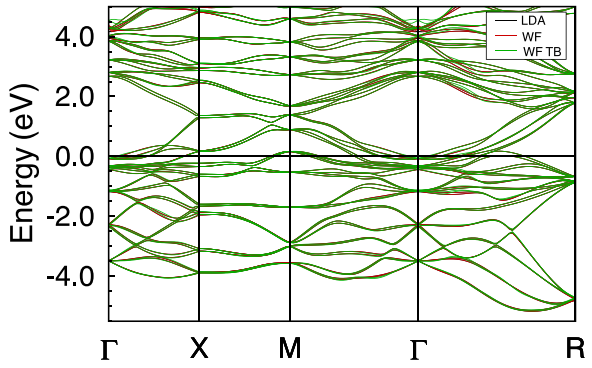

FIG. 8. Comparison of DFT band structure and Wannier fit with SOC.

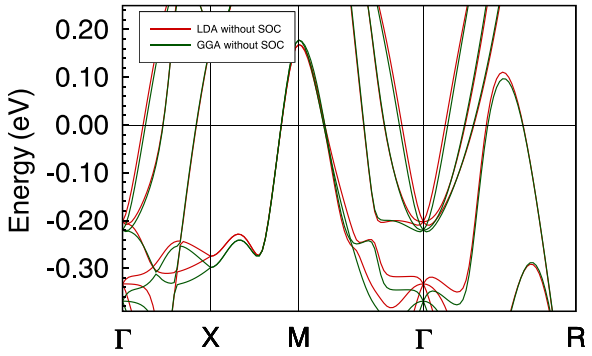

FIG. 9. Comparison of LDA and GGA band structures without SOC.

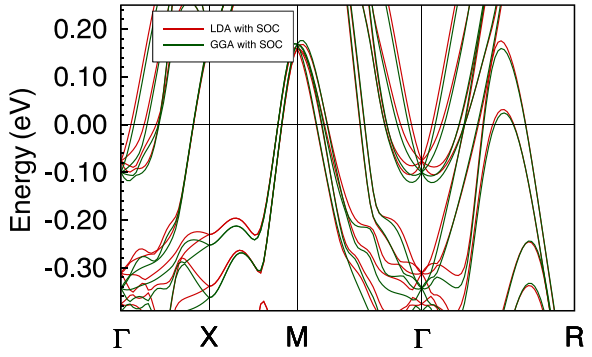

FIG. 10. Comparison of LDA and GGA band structures with SOC.

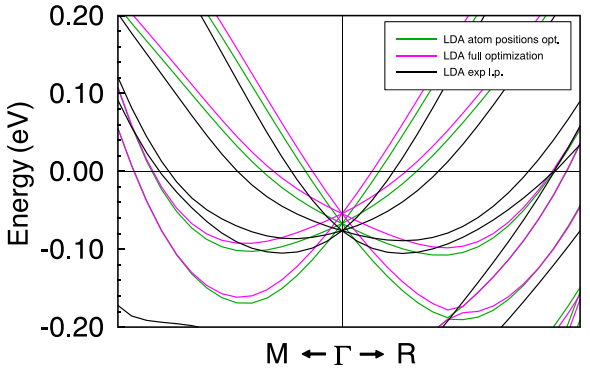

FIG. 11. Zoom around the E_F of LDA bands with SOC for Expt., atom positions optimized, and fully optimized structure.

and black curves are on top of each other in both figures in a given energy range). There exist minor deviations of the WF TB model from the DFT band structure. However, these are not of any relevance for the results presented in the current study. Good qualitative agreement of the DFT, WF, and WF TB band structures is strong evidence that all relevant hopping parameters are properly taken into account.

2. LDA versus GGA

In Figs. 9 and 10, we show a comparison of the band structures from LDA and GGA without and with SOC, respectively. While both functionals provide the same general description, the GGA eigenvalues are shifted down compared to the LDA values at our point of interest (Γ). The threefold degeneracy at Γ in the calculations with neglected SOC becomes fourfold and twofold degenerate with SOC, and it is lifted up in energy in both functionals.

3. Optimization of the Expt. structure

In Fig. 11, we compare the band structures obtained by two steps of crystal structure optimization (full and atomic coordinates only) with the experimental crystal structure.

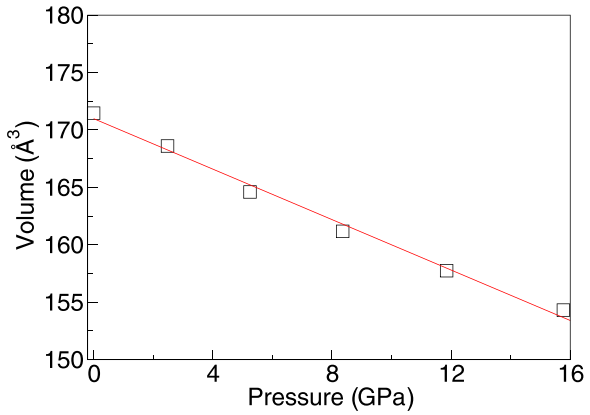

FIG. 12. Pressure dependence of the unit cell volume.

TABLE II. NN hopping parameters in eV for LDA calculations without SOC. The hopping parameters that are smaller than 0.25 eV are not presented in the table. The superscript indices stand for different hopping directions and the notation is according to Fig. 14 for nearest neighbors.

	Hf $5d_{xy}$	Hf $5d_{yz}$	Hf $5d_{z^2}$	Hf $5d_{xz}$	Hf $5d_{x^2-y^2}$	Hf $6p_y$	Hf $6p_z$	Hf $6p_x$
Sn $5p_y$	-1.17^g -1.11^e -0.49^c 0.46^f 0.42^a	0.48^a 0.26^f	0.87^d -0.86^g -0.77^e -0.75^b	0.81^a	-0.95^g 0.91^d	-1.70^g -1.47^d -0.55^a 0.36^c	-1.01^e -0.74^a 0.71^b -0.37^c	-0.78^d -0.65^a 0.60^g -0.36^b
Sn $5p_z$	0.81^a	-1.17^b -1.11^e -0.49^g 0.46^d 0.42^a	1.25^b -1.22^e 0.48^c 0.39^f	0.48^a 0.26^d	-0.67^f -0.59^c -0.27^b 0.29^e	-0.78^e -0.65^a 0.60^b -0.36^c	-1.70^b -1.47^e -0.55^a 0.36^g	-1.01^f -0.74^a 0.71^c -0.37^g
Sn $5p_x$	0.48^a 0.26^e	0.81^a	-0.39^c 0.38^d 0.36^f 0.27^g	-1.17^c -1.11^f -0.49^b 0.46^e 0.42^a	1.22^c -1.21^f 0.71^g 0.67^d	-1.01^d -0.74^a 0.71^g -0.37^b	-0.78^f -0.65^a 0.60^c -0.36^g	-1.70^c -1.47^f -0.55^a 0.36^b

TABLE III. NNN hopping parameters in eV for LDA calculations without SOC. The hopping parameters that are smaller than 0.25 eV are not presented in the table. The superscript indices stand for different hopping directions and the notation is according to Fig. 15 for next-nearest neighbors.

	Hf $5d_{xy}$	Hf $5d_{yz}$	Hf $5d_{z^2}$	Hf $5d_{xz}$	Hf $5d_{x^2-y^2}$	Hf $6p_y$	Hf $6p_z$	Hf $6p_x$
Hf $5d_{xy}$	$-0.43^{1,2}$	0.40^1 -0.28^5 0.26^2 0.25^4	-0.32^2	0.40^6 0.28^1 0.26^3 -0.25^2	0.31^3	0.76^1 0.67^2	-0.42^1 0.37^6 0.27^5	0.61^1 -0.54^2 -0.49^6 -0.33^3
Hf $5d_{yz}$	0.40^2 0.28^4 0.26^1 -0.25^5	$-0.43^{4,5}$	-0.30^4 0.30^5 -0.29^1	0.40^4 -0.28^6 0.26^5 0.25^3		0.61^4 -0.54^5 -0.49^2 -0.33^1	0.76^4 0.67^5	-0.42^5 0.37^2 0.27^6
Hf $5d_{xz}$	0.40^3 -0.28^2 0.26^6 0.25^1	0.40^5 0.28^3 0.26^4 -0.25^6		$-0.43^{3,6}$	0.36^6 -0.29^3	-0.42^3 0.37^5 0.27^2	0.61^3 -0.54^6 -0.49^5 -0.33^4	0.76^3 0.67^6
Hf $5d_{x^2-y^2}$	-0.31^6			-0.36^3 0.29^6		0.46^2 -0.42^1		0.53^3 -0.39^6
Hf $5d_{z^2}$	0.32^1	0.30^5 -0.30^4 0.29^2				-0.37^1	0.54^4 -0.49^5	0.30^6
Hf $6p_y$	-0.76^2 -0.67^1	0.61^5 -0.54^4 0.49^1 0.33^2	-0.37^2	-0.42^6 0.37^4 0.27^1	0.46^1 -0.42^2	$0.74^{1,2}$ $0.56^{4,5}$	0.49^4 -0.46^1 -0.45^5 0.27^2 -0.26^6	-0.49^2 0.46^6 0.45^1 -0.27^6 -0.26^4
Hf $6p_z$	-0.42^2 0.37^3 0.27^4	-0.76^5 -0.67^4	0.54^5 -0.49^4	0.61^6 -0.54^3 0.49^4 0.33^5		-0.49^5 0.46^2 0.45^4 -0.27^1 -0.26^3	$0.74^{4,5}$ $0.56^{3,6}$	0.49^3 -0.46^4 -0.45^6 0.27^5 -0.26^1
Hf $6p_x$	0.61^2 -0.54^1 0.49^3 0.33^6	-0.42^5 0.37^1 0.27^3	0.30^3	-0.76^6 -0.67^3	0.53^6 -0.39^3	0.49^1 -0.46^3 -0.45^2 0.27^6 -0.26^5	-0.49^6 0.46^5 0.45^3 -0.27^4 -0.26^1	$0.74^{3,6}$ $0.56^{1,2}$

TABLE IV. NN hopping parameters in eV for LDA calculations with SOC. The hopping parameters that are smaller than 0.25 eV are not presented in the table. The superscript indices stand for different hopping directions and the notation is according to Fig. 14 for nearest neighbors.

	Hf $5\tilde{d}_{xy}up$	Hf $5\tilde{d}_{yz}up$	Hf $5\tilde{d}_{z^2}up$	Hf $5\tilde{d}_{xz}up$	Hf $5\tilde{d}_{x^2-y^2}up$	Hf $6\tilde{p}_{y}up$	Hf $6\tilde{p}_{z}up$	Hf $6\tilde{p}_{x}up$
Sn $5\tilde{p}_{y}up$	-1.17^{g} $(-1.11^{d}+$ $i(-0.013))$ -0.49^{c} 0.47^{f} $0.42^{a}+$ $i(0.011)$	0.48^{a} 0.26^{c}	0.88^{d} -0.86^{g} -0.79^{e} -0.76^{b}	0.81^{a}	$(-0.96^{g}+$ $i(0.015))$ 0.92^{d}	-1.65^{g} -1.42^{d} $(-0.54^{a}+$ $i(-0.034))$ 0.38^{c}	$(-1.04^{e}+$ $i(0.015))$ $(-0.70^{a}+$ $i(-0.016))$ 0.69^{b} -0.39^{c}	$(-0.79^{d}+$ $i(-0.016))$ $(-0.64^{a}+$ $i(-0.015))$ 0.59^{g} $(-0.38^{b}+$ $i(-0.022))$
Sn $5\tilde{p}_{z}up$	0.81^{a}	-1.17^{b} -1.11^{e} -0.49^{g} 0.47^{d} 0.42^{a}	1.26^{b} -1.23^{e} 0.49^{c} 0.40^{f}	0.48^{a} 0.26^{d}	-0.68^{f} -0.59^{c} 0.30^{e} -0.27^{b}	-0.79^{e} -0.64^{a} 0.59^{b} $(-0.38^{c}+$ $i(0.020))$	-1.65^{b} -1.42^{e} -0.54^{a} 0.38^{g}	$(-1.04^{f}+$ $i(-0.011))$ -0.70^{a} $(0.69^{c}+$ $i(0.017))$ $(-0.39^{g}+$ $i(0.012))$
Sn $5\tilde{p}_{x}up$	$(0.48^{a}+$ $i(-0.026))$ 0.26^{e}	0.81^{a}	-0.40^{c} 0.39^{d} 0.36^{f} 0.27^{g}	$(-1.17^{c}+$ $i(0.013))$ -1.11^{f} -0.49^{b} 0.47^{e} 0.42^{a}	1.22^{c} -1.22^{f} 0.72^{g} $(0.68^{d}+$ $i(-0.018))$	$(-1.04^{d}+$ $i(0.041))$ $(-0.70^{a}+$ $i(0.031))$ $(0.69^{g}+$ $i(0.043))$ $(-0.39^{b}+$ $i(0.025))$	-0.79^{f} -0.64^{a} $(0.59^{c}+$ $i(-0.015))$ $(-0.38^{g}+$ $i(0.017))$	-1.65^{c} -1.42^{f} $(-0.54^{a}+$ $i(0.027))$ 0.38^{b}

4. Volume-pressure dependence

Figure 12 shows the calculated volume-pressure dependence for HfSn, obtained by making use of the inverse Birch-Murnaghan equation [41].

5. Berry curvature

Figure 13 shows the band-resolved and the Berry curvature (BC) summed over the occupied states. The color coding is according to the z component of the BC. We observe a large peak in the BC [Fig. 13(b)] originating from two almost degenerate bands at the E_F along the Γ-R direction. In addition, along the same direction, there are two smaller peaks originating from the bands in the vicinity of the Fermi level, created as a result of SOC.

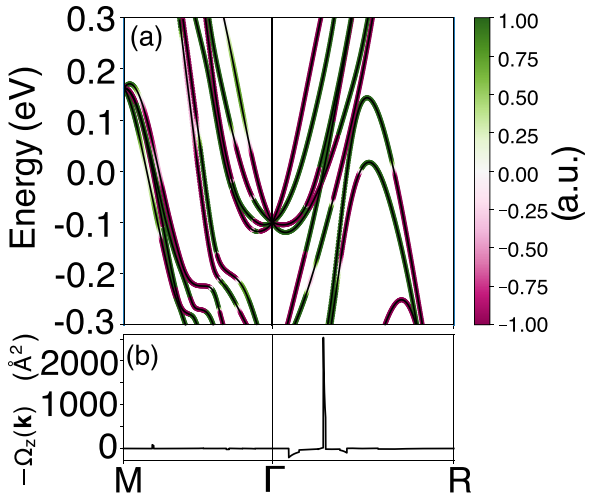

FIG. 13. (a) Band-resolved BC along M-Γ-R. (b) The BC summed over all occupied states below the Fermi energy for the same path.

6. Parameters of a tight-binding model

In the tables below, we provide hopping parameters for calculations with and without SOC. We report the nearest-neighbor and next-nearest-neighbor hopping parameters in Tables II and III, respectively, for calculations without SOC. In Tables IV and V, we list nearest- and

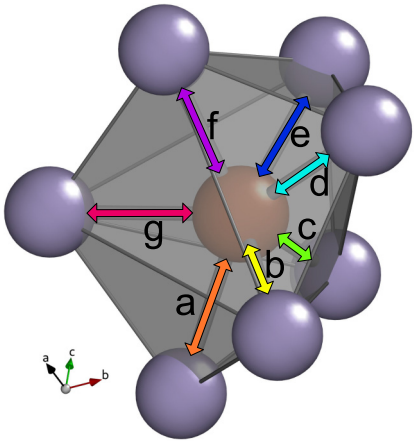

FIG. 14. NN polyhedron of the HfSn. The letters denote different hopping directions that can occur in the NN polyhedron.

TABLE V. NNN hopping parameters in eV for LDA calculations with SOC. The hopping parameters that are smaller than 0.25 eV are not presented in the table. The superscript indices stand for different hopping directions and the notation is according to Fig. 15 for next-nearest neighbors.

	Hf $5\tilde{d}_{xy}up$	Hf $5\tilde{d}_{yz}up$	Hf $5\tilde{d}_{z^2}up$	Hf $5\tilde{d}_{xz}up$	Hf $5\tilde{d}_{x^2-y^2}up$	Hf $6\tilde{p}_{y}up$	Hf $6\tilde{p}_{z}up$	Hf $6\tilde{p}_{x}up$
Hf $5\tilde{d}_{xy}up$	$-0.43^{1,2}$	0.40^{1} -0.28^{5} 0.26^{2} 0.25^{4}	-0.32^{2}	0.40^{6} 0.28^{1} 0.26^{3} -0.25^{2}	0.31^{3}	0.75^{1} 0.67^{2}	-0.43^{1} 0.36^{6} 0.26^{5} 0.25^{2}	0.61^{1} -0.54^{2} -0.49^{6} -0.33^{3}
Hf $5\tilde{d}_{yz}up$	0.40^{2} 0.28^{4} 0.26^{1} -0.25^{5}	$-0.43^{4,5}$	-0.31^{4} 0.30^{5} -0.29^{1}	0.40^{4} -0.28^{6} 0.26^{5} 0.25^{3}		0.61^{4} -0.54^{5} -0.49^{2} -0.33^{1}	0.75^{4} 0.67^{5}	-0.43^{4} 0.36^{2} 0.26^{6} 0.25^{5}
Hf $5\tilde{d}_{xz}up$	0.40^{3} -0.28^{2} 0.26^{6} 0.25^{1}	0.40^{5} 0.28^{3} 0.26^{4} -0.25^{6}		$-0.43^{3,6}$	0.36^{6} $(-0.29^{3}+$ $i(-0.011))$	-0.43^{3} 0.36^{5} 0.26^{2} 0.25^{6}	0.61^{3} -0.54^{6} -0.49^{5} -0.33^{4}	0.75^{3} 0.67^{6}
Hf $5\tilde{d}_{x^2-y^2}up$	-0.31^{6}			-0.36^{3} $(0.29^{6}+$ $i(0.011))$		0.47^{2} -0.41^{1}		0.52^{3} -0.39^{6}
Hf $5\tilde{d}_{z^2}up$	0.32^{1}	0.31^{5} -0.30^{4} 0.29^{2}				-0.37^{1}	0.54^{4} -0.50^{5}	0.31^{6}
Hf $6\tilde{p}_{y}up$	-0.75^{2} -0.67^{1}	0.61^{5} -0.54^{4} 0.49^{1} 0.33^{2}	-0.37^{2}	-0.43^{6} 0.36^{4} 0.26^{1} 0.25^{3}	0.47^{1} -0.41^{2}	$0.70^{1,2}$ $(0.52^{4,5}+$ $i(0.016))$	0.49^{4} $(-0.45^{5}+$ $i(-0.018))$ -0.43^{1} $(0.27^{2}+$ $i(-0.010))$ -0.25^{6}	$(-0.49^{2}+$ $i(-0.015))$ 0.45^{1} $(0.43^{6}+$ $i(0.013))$ -0.27^{3} -0.25^{4}
Hf $6\tilde{p}_{z}up$	-0.43^{2} 0.36^{3} 0.26^{4} 0.25^{1}	-0.75^{5} -0.67^{4}	0.54^{5} -0.50^{4}	0.61^{6} -0.54^{3} 0.49^{4} 0.33^{5}		-0.49^{5} $(0.45^{4}$ $i(-0.018))$ 0.43^{2} $(-0.27^{1}$ $i(0.010))$ -0.25^{3}	$0.70^{4,5}$ $0.52^{3,6}$	0.49^{3} -0.45^{6} -0.43^{4} 0.27^{5} $(-0.25^{2}+$ $i(-0.016))$
Hf $6\tilde{p}_{x}up$	0.61^{2} -0.54^{1} 0.49^{3} 0.33^{6}	-0.43^{5} 0.36^{1} 0.26^{3} 0.25^{4}	0.31^{3}	-0.67^{3} -0.75^{6}	0.52^{6} -0.39^{3}	$(0.49^{1}+$ $i(0.016))$ -0.45^{2} $(-0.43^{3}+$ $i(-0.013))$ 0.27^{6} -0.25^{5}	-0.49^{6} 0.45^{3} 0.43^{5} -0.27^{4} $(-0.25^{1}+$ $i(-0.016))$	$(0.70^{3,6}+$ $i(0.014))$ $0.52^{1,2}$

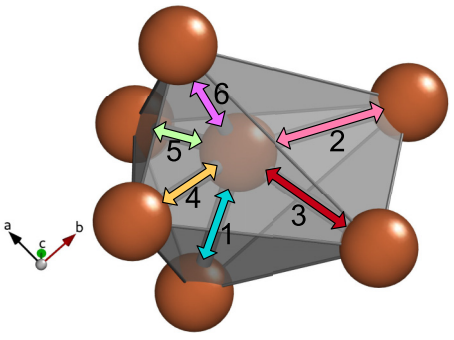

FIG. 15. NNN polyhedron of the HfSn. There are six possibilities for the hopping from one Hf to the neighboring ones, denoted with numbers from 1 to 6.

next-nearest-neighbor parameters, respectively, for calculations with SOC. The superscript indices stand for different hopping directions and the notation is according to Fig. 14 for nearest neighbors and Fig. 15 for next-nearest neighbors. Due to the fact that HfSn is not expected to show heavy relativistic effects, the full relativistic basis in calculations with SOC can be projected onto a $lm\sigma$ basis in a good approximation. To distinguish orbital projections in calculations without SOC and with SOC, for the latter case we employ the $\sim$ symbol above the orbitals.

[1] G. H. Fecher, J. Kübler, and C. Felser, Chirality in the solid state: Chiral crystal structures in chiral and achiral space groups, Materials **15**, 5812 (2022).

[2] A. Franciosi, D. J. Peterman, J. H. Weaver, and V. L. Moruzzi, Structural morphology and electronic properties of the Si-Cr interface, Phys. Rev. B **25**, 4981 (1982).

[3] V. Vescoli, L. Degiorgi, B. Buschinger, W. Guth, C. Geibel, and F. Steglich, The optical properties of RuSi: Kondo insulator or conventional semiconductor? Solid State Commun. **105**, 367 (1998).

[4] S. Datta, A. Vasdev, P. S. Rana, K. Motla, A. Kataria, R. P. Singh, T. Das, and G. Sheet, Spectroscopic evidence of multigap superconductivity in noncentrosymmetric AuBe, Phys. Rev. B **105**, 104505 (2022).

[5] S. Mühlbauer, B. Binz, F. Jonietz, C. Pfleiderer, A. Rosch, A. Neubauer, R. Georgii, and P. Böni, Skyrmion lattice in a chiral magnet, Science **323**, 915 (2009).

[6] N. B. M. Schröter, S. Stolz, K. Manna, F. de Juan, M. G. Vergniory, J. A. Krieger, D. Pei, T. Schmitt, P. Dudin, T. K. Kim, C. Cacho, B. Bradlyn, H. Borrmann, M. Schmidt, R. Widmer, V. N. Strocov, and C. Felser, Observation and control of maximal Chern numbers in a chiral topological semimetal, Science **369**, 179 (2020).

[7] Q. Yang, G. Li, K. Manna, F. Fan, C. Felser, and Y. Sun, Topological engineering of Pt-group-metal-based chiral crystals toward high-efficiency hydrogen evolution catalysts, Adv. Mater. **32**, 1908518 (2020).

[8] D. A. Pshenay-Severin and A. T. Burkov, Electronic structure of B20 (FeSi-type) transition-metal monosilicides, Materials **12**, 2710 (2019).

[9] O. Schob and E. Parthé, The structure of HfSn, Acta Crystallogr. **17**, 452 (1964).

[10] Q.-J. Hong and A. van de Walle, Prediction of the material with highest known melting point from *ab initio* molecular dynamics calculations, Phys. Rev. B **92**, 020104(R) (2015).

[11] L. Zhou, B. Shao, W. Shi, Y. Sun, C. Felser, B. Yan, and T. Frauenheim, Prediction of the quantum spin Hall effect in monolayers of transition-metal carbides *M*C (M = Ti, Zr, Hf), 2D Mater. **3**, 035022 (2016).

[12] Y. Gao, T. Iitaka, and Z. Li, Terahertz nonlinear optics of chiral semimetals RhSn, HfSn, and PdGa, Eur. Phys. J. B **94**, 95 (2021).

[13] A. Jain, S. P. Ong, G. Hautier, W. Chen, W. D. Richards, S. Dacek, S. Cholia, D. Gunter, D. Skinner, G. Ceder, and K. A. Persson, The materials project: A materials genome approach to accelerating materials innovation, APL Mater. **1**, 011002 (2013).

[14] Z.-Q. Huang, W.-C. Chen, G. Macam, C. Crisostomo, S.-M. Huang, R.-B. Chen, M. Albao, D.-J. Jang, H. Lin, and F.-C. Chuang, Predicition of quantum anomalous Hall effect in *M*Bi and *M*Sb (*M*: Ti, Zr, and Hf) honeycombs, Nanoscale Res. Lett. **13**, 43 (2018).

[15] I. A. Tsyganova, M. A. Tylkina, and E. M. Savitskiy, Sn-Hf and Sn-Re phase diagrams, Izv. Akad. Nauk SSSR, Met. **3**, 188 (1971) (in Russian).

[16] L. Romaka, Y. Stadnyk, and O. Bodak, Ternary Hf-Co-Sn system, J. Alloys Compd. **317-318**, 347 (2001).

[17] Y. Stadnyk and L. Romaka, Phase equilibria in the Hf–Ni–Sn ternary system and crystal structures of the Hf2Ni2Sn compound, J. Alloys Compd. **316**, 169 (2001).

[18] C. Tang, B. Hu, Y. Du, D. Zhao, P. Zhou, F. Zheng, Q. Gao, and J. Wang, Thermodynamic modeling of the Hf–Sn and Sn–Y systems, Calphad **39**, 91 (2012).

[19] K. Koepernik and H. Eschrig, Full-potential nonorthogonal local-orbital minimum-basis band-structure scheme, Phys. Rev. B **59**, 1743 (1999).

[20] G. Kresse and J. Hafner, *Ab initio* molecular dynamics for liquid metals, Phys. Rev. B **47**, 558 (1993).

[21] G. Kresse and J. Furthmüller, Efficiency of *ab initio* total energy calculations for metals and semiconductors using a plane-wave basis set, Comput. Mater. Sci. **6**, 15 (1996).

[22] G. Kresse and J. Furthmüller, Efficient iterative schemes for *ab initio* total-energy calculations using a plane-wave basis set, Phys. Rev. B **54**, 11169 (1996).

[23] J. P. Perdew and Y. Wang, Accurate and simple analytic representation of the electron-gas correlation energy, Phys. Rev. B **45**, 13244 (1992).

[24] J. P. Perdew, K. Burke, and M. Ernzerhof, Generalized gradient approximation made simple, Phys. Rev. Lett. **77**, 3865 (1996).

[25] D. M. Ceperley and B. J. Alder, Ground state of the electron gas by a stochastic method, Phys. Rev. Lett. **45**, 566 (1980).

[26] A. A. Mostofi, J. R. Yates, G. Pizzi, Y.-S. Lee, I. Souza, D. Vanderbilt, and N. Marzari, An updated version of WANNIER90: A tool for obtaining maximally localised Wannier functions, Comput. Phys. Commun. **185**, 2309 (2014).

[27] Q. Wu, S. Zhang, H.-F. Song, M. Troyer, and A. A. Soluyanov, WANNIERTOOLS: An open-source software package for novel topological materials, Comput. Phys. Commun. **224**, 405 (2018).

[28] S. Tsirkin, High performance Wannier interpolation of Berry curvature and related quantitites with WANNIERBERRI code, npj Comput. Mater. **7**, 33 (2021).

[29] L. Vočadlo, G. D. Price, and I. G. Wood, Crystal structure, compressibility and possible phase transitions in ε-FeSi studied by first-principles pseudopotential calculations, Acta Crystallograph. Sect. B **55**, 484 (1999).

[30] J. Klotz, K. Götze, T. Förster, J. A. N. Bruin, J. Wosnitza, K. Weber, M. Schmidt, W. Schnelle, C. Geibel, U. K. Rößler, and H. Rosner, Electronic band structure and proximity to magnetic ordering in the chiral cubic compound CrGe, Phys. Rev. B **99**, 085130 (2019).

[31] B. Bradlyn, J. Cano, Z. Wang, M. G. Vergniory, C. Felser, R. J. Cava, and B. A. Bernevig, Beyond Dirac and Weyl fermions: Unconventional quasiparticles in conventional crystals, Science **353**, aaf5037 (2016).

[32] N. Huber, K. Alpin, G. L. Causer, L. Worch, A. Bauer, G. Benka, M. M. Hirschmann, A. P. Schnyder, C. Pfleiderer, and M. A. Wilde, Network of topological nodal planes, multifold degeneracies, and Weyl points in CoSi, Phys. Rev. Lett. **129**, 026401 (2022).

[33] D. A. Pshenay-Severin, Y. V. Ivanov, A. A. Burkov, and A. T. Burkov, Band structure and unconventional electronic topology of CoSi, J. Phys.: Condens. Matter **30**, 135501 (2018).

[34] C. K. Barman, C. Mondal, S. Pujari, B. Pathak, and A. Alam, Symmetry protection and giant Fermi arcs from multifold fermions in binary, ternary, and quaternary compounds, Phys. Rev. B **102**, 155147 (2020).

[35] F. Tran, R. Laskowski, P. Blaha, and K. Schwarz, Performance on molecules, surfaces, and solids of the Wu-Cohen

GGA exchange-correlation energy functional, Phys. Rev. B **75**, 115131 (2007).

[36] B. Grabowski, T. Hickel, and J. Neugebauer, *Ab initio* study of the thermodynamic properties of nonmagnetic elementary fcc metals: Exchange-correlation-related error bars and chemical trends, Phys. Rev. B **76**, 024309 (2007).

[37] M. Hebbache and M. Zemzemi, *Ab initio* study of high-pressure behaviour of a low compressibility metal and a hard material: Osmium and diamond, Phys. Rev. B **70**, 224107 (2004).

[38] K. Choudhary, G. Cheon, E. Reed, and F. Tavazza, Elastic properties of bulk and low-dimensional materials using van der Waals density functional, Phys. Rev. B **98**, 014107 (2018).

[39] X. Bai, Y. Li, B. Xiao, Y. Rao, H. Liang, L. He, and J. Feng, Structural, mechanical, electronic properties of refractory Hf-Al intermetallics from SCAN meta-GGA density functional calculations, Mater. Chem. Phys. **254**, 123423 (2020).

[40] C.-L. Fu and K.-M. Ho, First-principles calculation of the equilibrium ground-state properties of transition metals: Applications to Nb and Mo, Phys. Rev. B **28**, 5480 (1983).

[41] F. D. Murnaghan, The compressibility of media under extreme pressures, Proc. Natl. Acad. Sci. USA **30**, 244 (1944).

[42] M. Barber, *Uniaxial Stress Technique and Investigations of Correlated Electron Systems* (Springer International, Cham, Switzeland, 2018), pp. 13–48.

[43] J. M. Ziman, *Models of Disorder: The Theoretical Physics of Homogeneously Disordered Systems* (Cambridge University Press, Cambridge, 1979).

[44] D. T. Son and B. Z. Spivak, Chiral anomaly and classical negative magnetoresistance of Weyl metals, Phys. Rev. B **88**, 104412 (2013).

[45] H. B. Nielsen and M. Ninomiya, The Adler-Bell-Jackiw anomaly and Weyl fermions in a crystal, Phys. Lett. B **130**, 389 (1983).

[46] Q. Yang, J. Xiao, I. Robredo, M. G. Vergniory, B. Yan, and C. Felser, Monopol-like orbital momentum locking and the induced orbital transport in topological chiral semimetals, Proc. Natl. Acad. Sci. USA **120**, e2305541120 (2023).

[47] F. de Juan, A. G. Grushin, T. Morimoto, and J. E. Moore, Quantized circular photogalvanic effect in Weyl semimetals, Nat. Commun. **8**, 15995 (2017).

[48] S. Kaushik and J. Cano, Magnetic photocurrents in multifold Weyl fermions, Phys. Rev. B **104**, 155149 (2021).